electronics

Article

A Fast Cross-Correlation Combined with Interpolation Algorithms for the LiDAR Working in the High Background Noise

Thanh-Tuan Nguyen [1,2,*], Ching-Hwa Cheng [3], Don-Gey Liu [1,3] and Minh-Hai Le [1]

[1] Ph.D. Program of Electrical and Communications Engineering, Feng Chia University, Taichung 40724, Taiwan; dgliu@fcu.edu.tw (D.-G.L.); lmhai@tvu.edu.vn (M.-H.L.)
[2] Department of Electronic Engineering, Kien Giang College, Rach Gia 91000, Vietnam
[3] Department of Electronic Engineering, Feng Chia University, Taichung 40724, Taiwan; chengch@fcu.edu.tw
* Correspondence: nttuan@kgc.edu.vn; Tel.: +866-958-414125

Abstract: Processing speed and accuracy of measurements are important factors reflecting the performance quality of light detection and ranging (LiDAR) systems. This study proposed a fast cross-correlation (fCC) algorithm to improve the computation loading in the LiDAR system operating in high background noise environments. To reduce the calculation time, we accumulated cycles of the receiver waveform to increase the signal-to-noise ratio. In this way, the stop pulse can be easily distinguished from the background noise by applying the cross-correlation (CC) on the accumulated receiver waveform with the first start pulse. In addition, the proposed fCC combined with variant interpolation techniques: the parabolic (fCCP), gaussian (fCCG), cosine (fCCC), and cubic spline (fCCS) to increase the measurement accuracy were also investigated and compared. The experiments were performed on the real-time LiDAR system under high background light intensity. The tested results showed that the proposed method fCCP achieved 879 ns per measurement, 38 times faster than the original CC method combined with the same parabolic interpolation algorithm (CCP) 33.5 µs. Meanwhile, the fCCS method resulted in the highest accuracy/precision, reaching 5.193 cm/8.588 cm, respectively. These results demonstrated that our proposed method significantly improves the measurements speed in the LiDAR system operating under strong background light.

Keywords: LiDAR; background noise; time-of-flight; cross-correlation; interpolation algorithms; execution time; accuracy and precision

check for updates

Citation: Nguyen, T.-T.; Cheng, C.-H.; Liu, D.-G.; Le, M.-H. A Fast Cross-Correlation Combined with Interpolation Algorithms for the LiDAR Working in the High Background Noise. *Electronics* **2022**, *11*, 985. https://doi.org/10.3390/electronics11070985

Academic Editor: Yide Wang

Received: 3 March 2022
Accepted: 22 March 2022
Published: 23 March 2022

Publisher's Note: MDPI stays neutral with regard to jurisdictional claims in published maps and institutional affiliations.

Copyright: © 2022 by the authors. Licensee MDPI, Basel, Switzerland. This article is an open access article distributed under the terms and conditions of the Creative Commons Attribution (CC BY) license (https://creativecommons.org/licenses/by/4.0/).

1. Introduction

The advanced driver assistance system (ADAS) is a fusion of many different sensors, including ultrasound, camera, radar, light detection and ranging (LiDAR), and global navigation satellite system, which is developed on a smart vehicle system to help car drivers perform complex driving missions and avoid dangerous situations. In particular, LiDAR plays an important role in detecting objects at long distances, accurately measuring distances, and building 2D and 3D images with high resolutions in harsh environmental conditions [1–8].

The working principle of LiDAR is based on the light reflection of a near-infrared short-wavelength laser beam to detect objects [9,10]. Therefore, it is greatly affected in environmental conditions with high background light intensity, such as electric lights and sunlight, which need to design noise handling systems in LiDAR to achieve high accuracy. Some hardware improvement methods have been studied. For example, the orbital angular momentum laser light transmission technique combines a photon sieve diffractive filter to separate scattered sunlight from the laser light is suggested in [11]; a noise reduction method to improve LiDAR performance based on a differential optical path is presented

in [12,13]; an adaptive photon coincidence detection remove background light in the single-photon avalanche diode (SPAD) sensor LiDAR is proposed in [14]. However, the hardware designs usually lead to a complex system and increasing costs. The second solution is to apply digital signal processing algorithms. For instance, de-noising the LiDAR signal by the variant mode decomposition combined with a whale optimization algorithm is proposed in [15], noise improvement by three different digital filtering methods the finite response low pass filter, the empirical mode decomposition filter, and Savitzky–Golay is suggested in [16], multi-class support vector machines and artificial neural network methods are compared in [17], and an approach to predict the performance of LiDAR in sunlight using the dimensionless parameter is implemented in [18]. The compound software algorithms also increase the execution time and significantly reduce the resolution of LiDAR, which are challenges for LiDAR system designers [2,10,19,20].

Time of flight (ToF) is an important technique for estimating the time delay between transmitted and received signals. It has been applied widely in measurement fields, such as blood velocity measurement [21], calculation of thickness in oil pipelines [22], non-contact thermometer [23], distance estimation and object detection in LiDAR [24–26], radar [27], and ultrasound systems [28,29]. ToF methods are classified into two approaches, directly ToF (DToF) and indirectly ToF (IToF). DToF technique uses pulse detection methods, such as the leading edge, peak detection, center of gravity, inflection discriminator, and constant fraction, to construct a histogram. The time delay value in DToF is the position of the bin with the largest amplitude (maximum count) [24–26,30–32] (pp. 243–249). These pulse detection methods perform quickly and accurately under ideal conditions with low background noise. However, since LiDAR often works in environments with high background noise and bad weather, causing the amplitude and width of the stopping pulse to be distorted and overlapped, the pulse detection methods are greatly affected and ineffective [20,30,33]. IToF algorithm is applied to signals in the full waveform. Cross-correlation (CC) is an IToF method of time delay estimation that relies on the maximum correlation coefficient between the transmitted and received signals. Compared with pulse detection methods, the CC applies more effectively in measurement systems operating in high noise environments [20,34–37]. One disadvantage of the CC method is that it is applied to signals in a full waveform, so this algorithm needs to process a large amount of data. Moreover, in bad weather conditions, the received signals contain a lot of noise, distorted or lost. Therefore, the methods for determining DToF as well as IToF must apply a transmitted pulse sequence that has more than one emitted pulse in the measurement to accurately determine the stop pulse [20,24–26]. Therefore, this study increases the execution time of the measurement, which leads to a decrease in the system resolution. To cover this problem, we proposed the fast cross-correlation (fCC) method to improve the processing speed of the LiDAR system, which is presented in Section 3.2.

The basic ToF determination methods do not increase the resolution or the accuracy of the measurement. Using a high-resolution analog-to-digital converter (ADC), the system will achieve high accuracy. However, this solution raises the cost, and the increased number of samples also affects the computational speed of the system. Some methods that combine CC with reduced interpolation algorithms significantly improve the accuracy of measurements, such as parabolic, gaussian, cosine, and cubic spline, and are presented in [38–41]. However, implementation in real-time LiDAR systems also affects the system's processing speed, which needs to be investigated to have an appropriate method selection.

In this paper, we proposed the fCC algorithm developed from the CC method to improve the execution time of measurements in the LiDAR system working under high background noise ambient. In addition, the four interpolation techniques parabolic, gaussian, cosine, and cubic spline combined with fCC to improve accuracy are applied and assessed. To prove the effectiveness of the proposed methods and investigate the accuracy of the interpolation methods and the effects of applying these methods to the processing time, we utilized the single-beam LiDAR system designed from our previous study [20].

The experiments were performed outdoors with strong background light intensity and set up at varying distances from 10 m to 140 m.

The article is organized into six sections. Section 1 introduces the motivation, importance of the LiDAR system, and related works. The structure of the LiDAR system and the initialization of the experiments are presented in Section 2. The proposed methods are shown and explained in Section 3. The experimental results demonstrating the proposed methods' efficiency in processing speed, accuracy, and precision are evaluated and compared in Section 4. The discussion of the obtained results is presented in Section 5. Finally, the conclusions are provided in Section 6.

2. LiDAR System and Initial Experiments

2.1. The Structure of LiDAR and Specifications

The LiDAR system used in this experiment was designed from our previous research [20]. The system's structure consists of three main blocks, as shown in Figure 1, including the signal generator system, the signal receiver unit, and the digitizing and data processing unit. We used a personal computer (PC) to display the results. In this study, we performed experiments at ranges reach 140 m, so the rangefinder was replaced by another that can measure up to 200 m with an accuracy of ±5 mm [42]. The start signal is modulated by the function generator (FG) in the form of a narrow pulse with a frequency of 1 MHz and then fed to the laser diver board to drive the diode laser to achieve an average output power of 2 mW. The emitted laser beam is collimated by an aspherical lens to reach a width of 2.3 mm. In the receiver unit, to limit the amount of light interference from the outside, we used the single-photon avalanche diode (SPAD) sensor with a small active area, a focus lens, and a filter lens to capture the reflected signal from the target. The signal emitted from the FG and the signal received from the sensor is synchronously digitized by two analog-to-digital converters (ADCs) with a sampling rate of 125 Mega samples per second (Msps). After the processing unit performed the distance calculation, the results were displayed on the PC. The specifications of the LiDAR system are described in detail in Table 1.

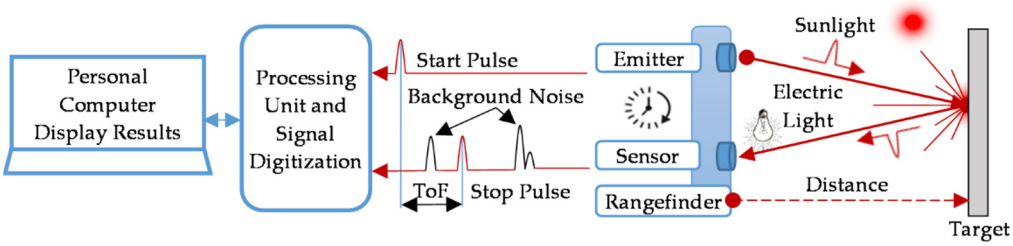


Figure 1. Block diagram and working principle of LiDAR.

2.2. The Waveforms Obtained at Different Light Intensities

In this study, in order to accurately evaluate the effect of background light noise in the real environment, we performed experiments outdoors with the target was a white paper in two cases: (i) at night with background noise sources from electric lights and (ii) at noon with strong background noise from the sunlight. The waveforms obtained in the two cases (i) and (ii) are shown in Figure 2a,b, respectively. Hardware-based solutions are adopted to limit the amount of background noise from the surrounding environment by using a sensor with a small active area, a focus lens with a limited diameter, and a bandpass filter lens [20]. However, observation of the obtained signals in Figure 2 in one start pulse (one cycle) shows that the received signal contains a lot of random stop pulses due to background light noise from electric lights and sunlight. The signal-to-noise ratio (SNR) is calculated from Formula (6) [20], case (i) is SNR = −3 dB and case (ii) is SNR = −9.1 dB. Therefore, we proposed software-based solutions to combat the effect of background light noise. The solutions are presented in the below sections.

Table 1. Specifications of the LiDAR system.

Parameters	Specifications
1. Emitting block	
Emitted frequency	F = 1 MHz
Pulse width	20 ns
Diameter of aspheric lens	6.35 mm
Focal of aspheric lens	3.1 mm
Peak power of laser	250 mW
Average power of laser	2 mW
Wavelength of laser	650 nm
Width of laser beam	2.53 mm
2. Received block	
SPAD sensor	Single-pixel
Active area of sensor	314 μm^2
Focal lens	60 mm
Diameter of focus lens	25.4 mm
Field of view angle	0.024°
Bandpass filter lens	650 nm
3. Signal processing block	
Embedded platform	Red Pitaya STEM Lab 125-14
Processor unit	ARM cortex A9, 667 MHz
Ram memory	512 MB
Sampling rate of ADCs	f_s = 125 Msps
Operating system	A lightweight version of Linux

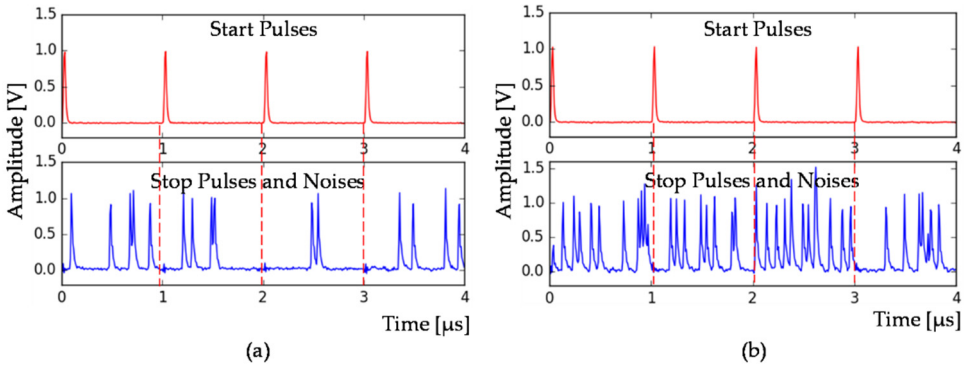


Figure 2. The start and stop signals are acquired in two outdoor instants: (**a**) at night with SNR of −3 dB; (**b**) at noon with SNR of −9.1 dB.

3. Proposed Methods

In this section, we present our approach to increase the measurement performance and accuracy of the LiDAR system based on cross-correlation (CC) methods. First, in Section 3.1, the original CC was reviewed from our previous study. Then, in Section 3.2, we present the proposed fast cross-correlation (fCC) algorithm based on the CC method to determine time-of-flight for the LiDAR-Pulse. Finally, four algorithms, which were elaborated from the fCC combined with corresponding interpolation methods including parabolic (fCCP), gaussian (fCCG), cosine (fCCC), and cubic spline (fCCS) to increase the accuracy of the measurements, are introduced in Section 3.3.

3.1. The Original Cross-Correlation

The original cross-correlation (CC) method determined time-of-flight (ToF) and relied on the cross-correlation function (CCF) to find the maximum correlation coefficients between two emitting and receiving signals in the full waveform. The CCF in the continuous-time form is determined by Formula (1), and the discrete-time form is given by Formula (2).

The ToF_d is the value index with the largest correlation coefficient of the CCF identified by Formula (3) [34,38,40,41].

$$x(\tau) = s_r(t) * s_e(t) = \int_{-\infty}^{\infty} s_r(t).s_e(t - \tau)dt \quad (1)$$

$$x[n] = \sum_{i=1}^{N} s_r[i].s_e[i - n],\ (n = -(N - 1), \ldots 0, \ldots, (N - 1)) \quad (2)$$

$$ToF_d = \arg[x_m] = \arg[\max(x[n])] \quad (3)$$

where s_e and s_r are emitting and receiving signal, respectively; x_m is the peak value of CCF; N is the total samples (length) of signal.

Our previous test results showed that in order to achieve a 100% success rate of measurements under strong background noise of −9.1 dB, the system needed to perform 20 transmitted pulses per frame in one measurement. The procedure for determining ToF applied by the conventional CC method is shown in Figure 3. A segment of 20 start pulses and corresponding stop pulses is shown in Figure 3a. In the LiDAR system, we used two analog-to-digital converters (ADCs) with a sampling rate of 125 Msps to capture the start and stop signal with the emitted signal frequency is 1 MHz. Hence, each cycle of the signal transmitting and receiving digitized by the ADCs is 125 samples. For 20 cycles, we needed 2500 samples for each start and stop channel. Formula (2) was applied to determine the correlation coefficients of two signals in the digital domain, and the results are given in Figure 3b. The ToF_d value is estimated directly by Formula (3) and presented in Figure 3c.

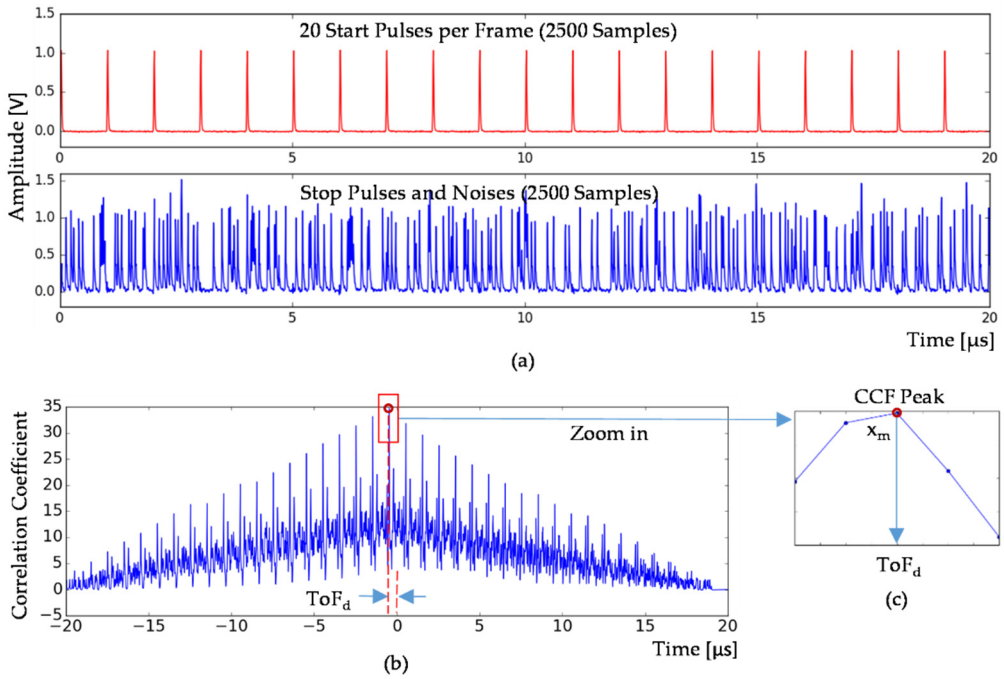


Figure 3. Estimating ToF_d by original CC method: (**a**) a frame 20 start and stop pulses; (**b**) correlation coefficients of the start and stop signals; (**c**) peak value x_m of the CCF, and ToF_d.

3.2. Fast Cross-Correlation (fCC)

To improve the calculation speed of measurements in a high noise environment, we proposed the fCC method, which is implemented in two steps as follows:

- Step 1: Add stop signals to determine the correct stop pulse from background noises.

The start pulses are transmitted at a fixed frequency (1 MHz). In the same measurement distance, the stop pulses are delayed at the same positions in each cycle. In contrast, light noise from the environment occurs randomly in every period. Based on these properties,

we separate the signal in Figure 3a into 20 emitted pulses and the corresponding stop signals, shown in Figure 4a. Then, we add parallel samples at the respective indexes of the 20 stop signals to determine the exact stop pulse position. The process of adding stop signals is calculated by Formula (4), and the result is shown in Figure 4b.

$$s_{stop}[k] = \sum_{j=1}^{20} s_{r(j)}[k],\ (k = 0,\ 1,\ 2,\ \ldots,\ 124) \tag{4}$$

where $s_{stop}[k]$ is the sum of 20 stop signals at the kth sample; $s_{r(j)}[k]$ is the kth sample of the jth stop signal.

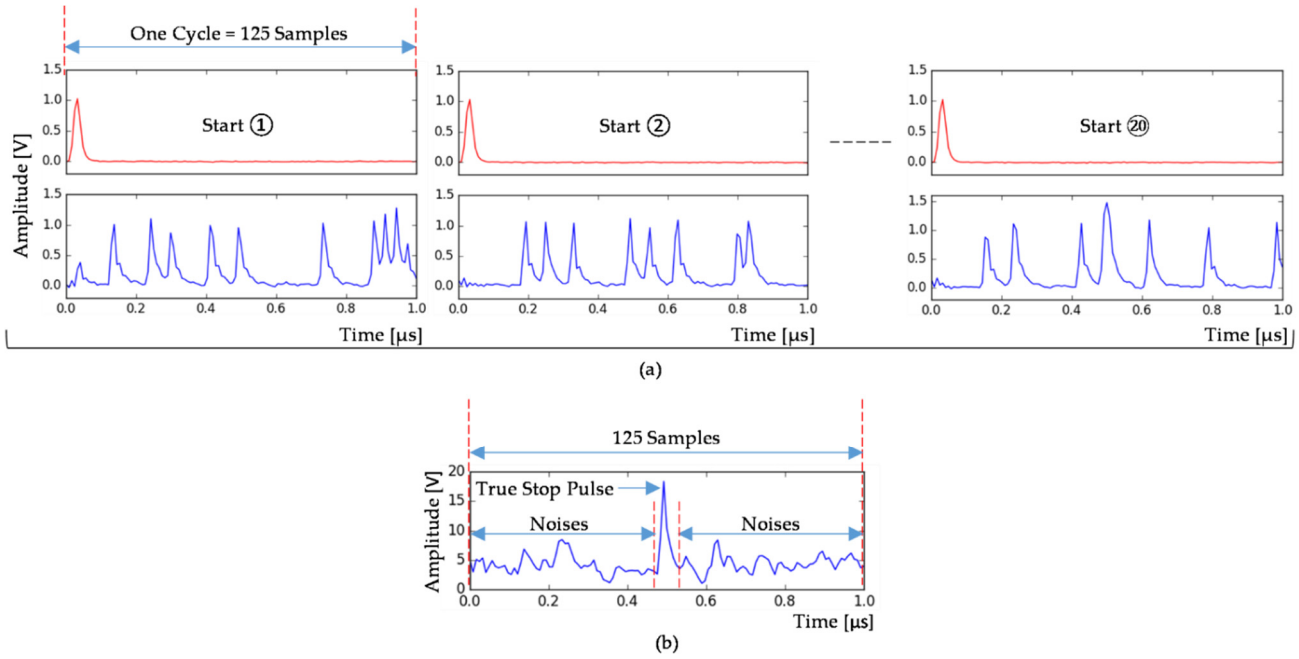


Figure 4. Parallel addition of stop signals; (**a**) twenty start signals and corresponding stop signals are separated; (**b**) sum of stop signals in twenty respective emitted pulses.

- Step 2: Implement the cross-correlation function (CCF) on the reduced start signal with the sum of the stop signals $s_{stop}[k]$.

One advantage of LiDAR-Pulse is the start pulses are very narrow and the same waveform in each cycle. Every emitted pulse cycle digitized by the analog-to-digital converter is 125 samples, where the narrow pulse is only in the first 10 samples, and the remaining 115 samples have values close to zero shown in Figure 5a. Moreover, the ToF_d value is the peak of the CCF. Therefore, we propose to apply the CCF (2) to a narrow pulse segment (first 10 samples) of the emitted pulse and the sum of 20 stop signal $s_{stop}[k]$ (125 samples) as shown in Figure 5a. The ToF_d value is estimated by Formula (3), and the result is depicted in Figure 5b,c.

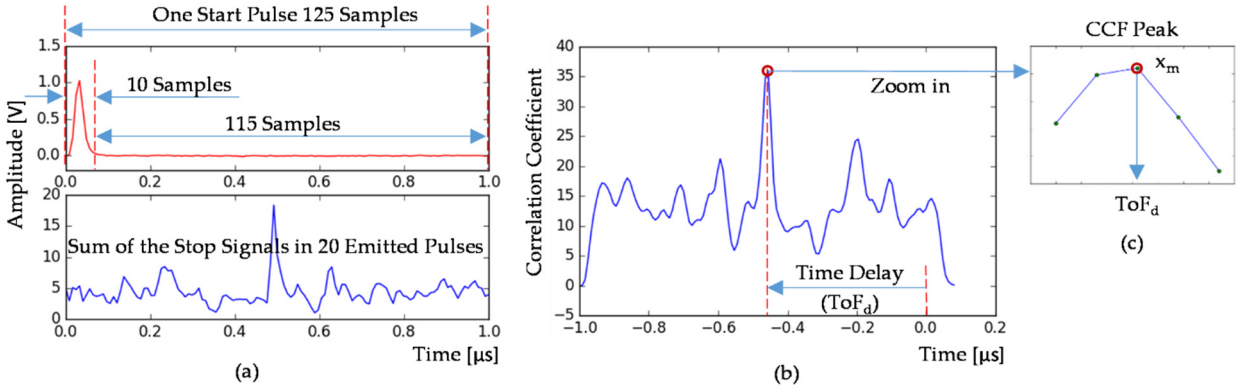


Figure 5. Determinating ToF_d by the proposed fCC method; (**a**) the narrow pulse start ten samples and the sum of the top signals; (**b**) correlation coefficients and ToF_d value obtained; (**c**) peak value x_m of the CCF.

In summary, let us show how the processing speed is improved by using the fCC method. Originally, the cross-correlation (CC) method was needed to perform the CCF between the start and stop signals with the same length of 2500 samples. This means that the algorithm needs to calculate 2500 × 2500 = 6,250,000 multiplication and 2499 × 2499 = 6,245,001 addition operations. With the proposed fCC method, step 1 implements 125 × 20 = 2500 addition operations, and step 2 executes the correlation function between the narrow start pulse of 10 samples and a stop signal of 125 samples. Thus, step 2 performs 125 × 10 = 1250 multiplication and 124 × 9 = 1116 addition operations. Totally, in two steps, fCC only performs 1250 multiplication and 3616 addition operations. Compared with CC, the fCC method has a very large reduction in the number of calculations, which proves that the proposed method greatly improves the system's processing speed.

3.3. Combining the Fast Cross-Correlation (fCC) with Interpolation Algorithms

In the LiDAR system, analog-to-digital converters (ADCs) are used for digitizing the signals, which have the higher the sampling rate, the higher the accuracy. However, this leads to increased computations due to the rising number of samples, and ADCs are more expensive. To solve these problems, we utilized ADCs 125 Msps with a limited resolution of 8 ns/sample equivalent to a minimum range error of ±1.2 m. Therefore, applying digital signal processing algorithms to improve accuracy is necessary. However, using these solutions reduce the system's processing speed. Hence, this study experimented and evaluated the execution time and accuracy indicators of four best-performing interpolation algorithms, including parabolic, gaussian, cosine [38,40], and cubic spline [39,43,44], combined with the proposed method fCC.

3.3.1. Combining the fCC with Parabolic (fCCP), Gaussian (fCCG), and Cosine (fCCC) Interpolation

The parabolic (5), gaussian (7), and cosine (9) functions applied similarly at the same three largest points of the correlation coefficients x_{m-1}, x_m, and x_{m+1} is shown in Figure 6. The subsample shift δToF_p, δToF_g, and δToF_c values are the double solution of the parabolic, gaussian, and cosine curves calculated by Equations (6), (8), and (10) respectively, is given by [40].

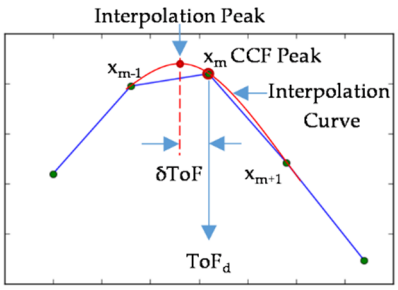


Figure 6. The peak position of the interpolation curves and the CCF.

- Parabolic Function (5) and interpolation Formula (6):

$$x_p(\tau) = a\tau^2 + b\tau + c \tag{5}$$

$$\delta ToF_p = -\frac{b}{2a} = \frac{x_{m-1} - x_{m+1}}{2f_s(x_{m-1} - 2x_m + x_{m+1})} \tag{6}$$

- Gaussian Function (7) and interpolation Formula (8):

$$x_g(\tau) = a \cdot \exp\left(-b(\tau - c)^2\right) \tag{7}$$

$$\delta ToF_g = -\frac{c}{f_s} = \frac{\ln(x_{m+1}) - \ln(x_{m-1})}{f_s(4\ln(x_m) - 2\ln(x_{m-1}) - 2\ln(x_{m+1}))} \tag{8}$$

- Cosine Function (9) and interpolation Formula (10):

$$x_c(\tau) = a \cdot \cos(\omega_0 \tau + \theta) \tag{9}$$

$$\delta ToF_c = -\frac{\theta}{f_s \omega_0},\ \omega_0 = \arccos\left(\frac{x_{m-1} + x_{m+1}}{2x_m}\right),\ \theta = \arctan\left(\frac{x_{m-1} - x_{m+1}}{2x_m \sin\omega_0}\right) \tag{10}$$

where ω_0 is angular frequency and θ is phase.

After applying the interpolation algorithms, the ToF value is the sum of ToF_d and δToF (δToF_p, or δToF_g, or δToF_c), which is determined by Formula (11)

$$ToF = ToF_d + \delta ToF \tag{11}$$

3.3.2. Combining the fCC with Cubic Spline Interpolation (fCCS)

The cubic spline interpolation method uses cubic polynomials to find new points in the boundary of a set of at least four known points to increase the resolution of the curves ([45], pp. 182–190), ([46], pp. 297–300). Applying the full-waveform increases the system execution time and is unnecessary. Therefore, we only interpolate at the five top points of the cross-correlation function (CCF) to improve the accuracy of the measurements. The cubic spline interpolation function is given by Formula (12).

$$x(\tau) = a\tau^3 + b\tau^2 + c\tau + d \tag{12}$$

Apply five maximum points of CCF x_{m-2}, x_{m-1}, x_m, x_{m+1}, and x_{m+2} as shown in Figure 7a, we have four fit cubic splines are given by:

$$x_1(\tau) = a_1\tau^3 + b_1\tau^2 + c_1\tau + d_1,\ (\tau_1 \le \tau \le \tau_2) \tag{13}$$

$$x_2(\tau) = a_2\tau^3 + b_2\tau^2 + c_2\tau + d_2,\ (\tau_2 \le \tau \le \tau_3) \tag{14}$$

$$x_3(\tau) = a_3\tau^3 + b_3\tau^2 + c_3\tau + d_3,\ (\tau_3 \le \tau \le \tau_4) \tag{15}$$

$$x_4(\tau) = a_4\tau^3 + b_4\tau^2 + c_4\tau + d_4,\ (\tau_4 \le \tau \le \tau_5) \tag{16}$$

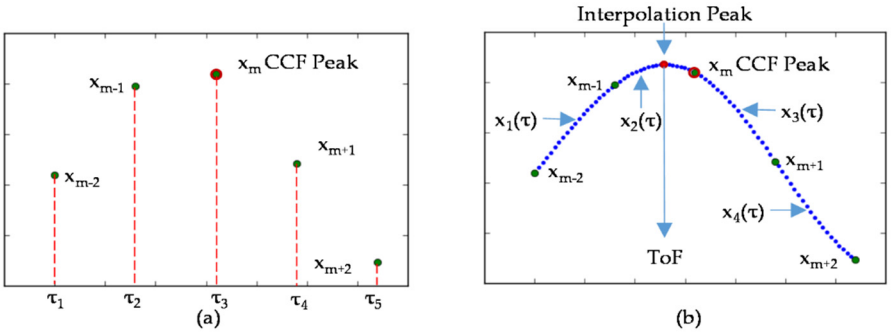


Figure 7. The procedure of determining interpolated peak by the cubic spline method; (**a**) the five maximal points of the CCF; (**b**) interpolated peak position and ToF value obtained.

To find the interpolation functions, we need to determine sixteen coefficients a_i, b_i, c_i, and d_i $(i = 1, 2, 3, 4)$ for the cubic Functions (13)–(16). Every cubic spline goes through two consecutive points (x_{m-2}, x_{m-1}), (x_{m-1}, x_m), (x_m, x_{m+1}), (x_{m+1}, x_{m+2}), so we have eight equations:

$$x_i(\tau_i) = a_i\tau_i^3 + b_i\tau_i^2 + c_i\tau_i + d_i, \ (i = 1, 2, 3, 4) \tag{17}$$

$$x_i(\tau_{i+1}) = a_i\tau_{i+1}^3 + b_i\tau_{i+1}^2 + c_i\tau_{i+1} + d_i, \ (i = 1, 2, 3, 4) \tag{18}$$

The first derivative of cubic splines at the three intersection points x_{m-1}, x_m, and x_{m+1} is equal and the same for the second derivative. Based on this property, we have six equations:

$$x_i'(\tau_{i+1}) = x_{i+1}'(\tau_{i+1}), \ (i = 1, 2, 3) \tag{19}$$

$$x_i''(\tau_{i+1}) = x_{i+1}''(\tau_{i+1}), \ (i = 1, 2, 3) \tag{20}$$

Apply "natural spline" boundary conditions, which the second derivative at the start and end points is zero to find the last two equations:

$$x_1''(\tau_1) = 0 \tag{21}$$

$$x_4''(\tau_5) = 0 \tag{22}$$

with the sixteen equations presented above, we found the coefficients a_i, b_i, c_i, and d_i $(i = 1, 2, 3, 4)$, then substituted them to the four interpolation functions in (13), (14), (15), and (16). Based on four finished interpolation functions, which can interpolate arbitrary points in the segment from x_{m-2} to x_{m+2}. The higher the number of interpolated points, the higher the resolution and accuracy. However, the number of calculations is very large, which affects the system's processing speed. Our experimental results showed that interpolating 80 points from five points x_{m-2}, x_{m-1}, x_m, x_{m+1}, and x_{m+2} gives the most accurate results. ToF is the index at the maximum value of the interpolation points, determined by Formula (23) and shown in Figure 7b.

$$\text{ToF} = \arg[\max(x[\tau])] \tag{23}$$

$$\text{Distance} = \frac{c \times \text{ToF}}{2}, \text{ where c is speed of the light} \tag{24}$$

The flowchart depicts the distance determination algorithm of the LiDAR system by the proposed method fCC combined with interpolation methods, which consists of five steps in Figure 8. Step one synchronously captures n start and stop signals by ADCs 125 Msps. Step two performs parallel addition of n stop signals (including noise) to determine the true stop pulse and background noise. Step three applies the correlation function to the narrow pulse segment (10 samples) of the start signal and the sum of n stop signals (125 samples). Step four combines parabolic, gaussian, cosine, or cubic spline interpolation algorithms to improve the accuracy of the measurements. The final step estimates the ToF value, and the distance is calculated by Formula (24).

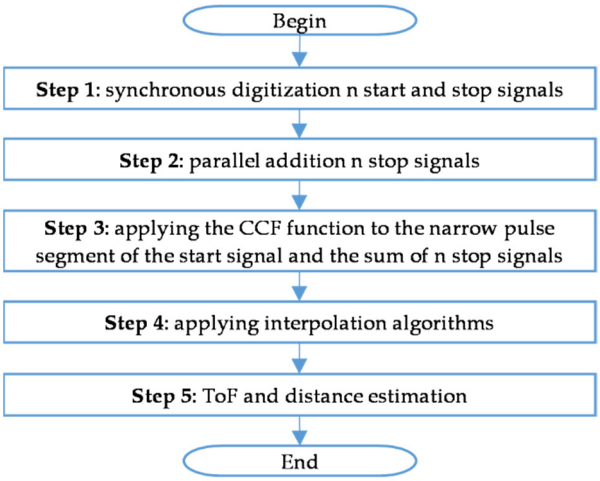


Figure 8. The flowchart describes the procedure for determining ToF and distance of the proposed fCC method combined with interpolation algorithms.

4. Experimental Results

To demonstrate the effectiveness of the proposed method and assess the interpolation methods, we perform experiments with LiDAR system in ambient with different background light intensities. Experiments setup and evaluation methods are presented in Section 4.1. The execution time results of the proposed algorithms are shown in Section 4.2. Comparisons of accuracy are mentioned in Section 4.3. Precision is described in Section 4.4. Finally, Section 4.5 compares the results with the performance of commercial LiDARs and recent research.

4.1. Installed Experiments and Evaluation Methods

The experiments shown in Figure 9 were carried out outdoors in two cases, as presented in Section 2.2: case (i) in Figure 9a performed at night with a signal-to-noise ratio (SNR) of −3 dB; case (ii) in Figure 9b tested at noon with an SNR of −9.1 dB. In each experiment, we changed the target range from 10 m to 140 m, for each step is 10 m. We performed 1000 times for each distance and applied all instants to ensure measurement reliability. The methods tested in this study included the original cross-correlation combined with the parabolic (CCP) method and the four proposed methods fCCP, fCCG, fCCC, and fCCS. The applied evaluation parameters were execution time, accuracy (or mean range error), and precision (or standard deviation) [20,30,47]. The accuracy is the average value of the total error magnitude of the measurement and its actual value in the defined number of measures, which is determined by Equation (25). The precision represents the system's random errors calculated from the standard deviation of the measurements in Equation (26).

$$\varepsilon_{acu} = \frac{1}{M}\sum_{i=1}^{M}|m_i - m_{act}| \tag{25}$$

$$\varepsilon_{pre} = \sqrt{\frac{1}{M}\sum_{i=1}^{M}(m_i - m_{avg})^2} \tag{26}$$

where ε_{acu} and ε_{pre} are respectively accuracy and precision of measurements, M is the total number of measurements at the same distance, m_i is the measured value at the *i*th times, m_{act} is the actual value measured from the reference rangefinder, and m_{avg} is the average of the measurements.

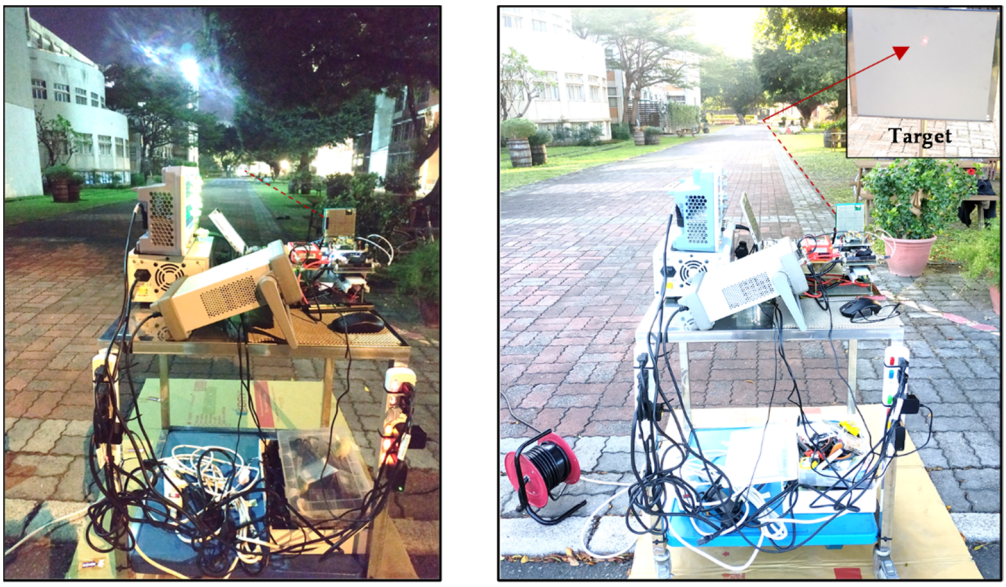
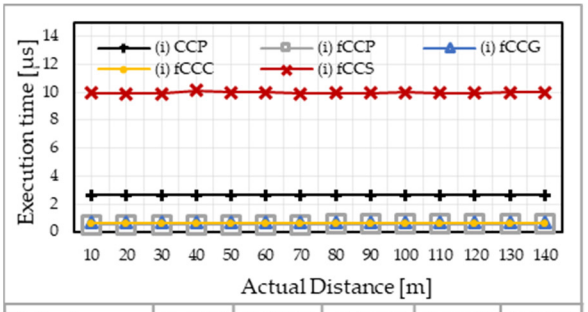


Figure 9. Pictures of the experimental setup: (**a**) outdoor at night; (**b**) outdoor at noon.

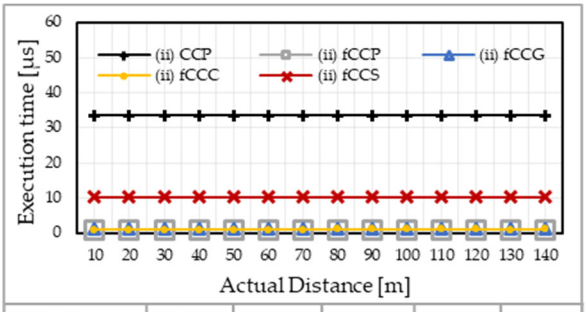
4.2. Comparing the Execution Time

From our experimental results, to achieve a 100% success rate of the measurements, it is necessary to apply five transmitted pulses per frame in case (i) and 20 transmitted pulses per frame in case (ii). The execution time results of the five methods CCP, fCCP, fCCG, fCCC, and fCCS are presented in Figure 10. Experimental case (i) in Figure 10a shows that the original CCP method has an average execution time of 2.627 µs is slower than the proposed methods fCCP, fCCG, and fCCC, which reach 0.539 µs, 0.652 µs, and 0.614 µs, respectively. Apart from that, the fCCS method has the slowest execution time of 9.962 µs. Figure 10b describes the results of case (ii), in which the CCP has the longest execution time of 33.5 µs, and three proposed methods with the fastest processing speed fCCP, fCCG, and fCCC reach 0.879 µs, 0.988 µs, and 0.965 µs, respectively.



Methods	(i) CCP	(i) fCCP	(i) fCCG	(i) fCCC	(i) fCCS
Mean Time (µs)	2.627	0.539	0.652	0.614	9.962

(a)



Methods	(ii) CCP	(ii) fCCP	(ii) fCCG	(ii) fCCC	(ii) fCCS
Mean Time (µs)	33.5	0.879	0.988	0.965	10.247

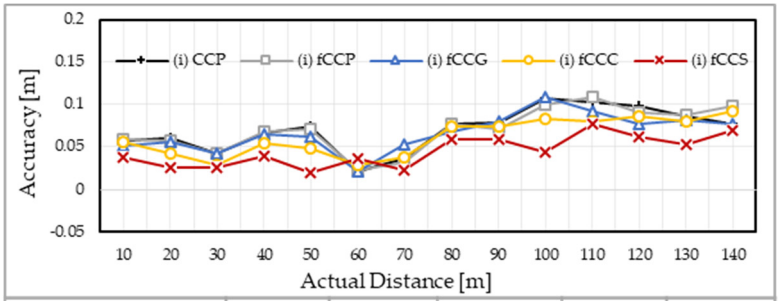
(b)

Figure 10. The execution time of the conventional CCP method and four proposed methods fCCP, fCCG, fCCC, and fCCS in two experimental instants: (**a**) outdoor at night; (**b**) outdoor at noon.

These experimental results showed that the proposed method fCCP, fCCG, and fCCC has an average execution time four times faster than the conventional method CCP in case (i) and is 34 times faster in case (ii). The processing time of the fCCS method is slower than the CCP in experiment (i) because the number of calculations in the cubic spline interpolation algorithm is quite large. However, fCCS is still three times faster than CCP in the experiment (ii).

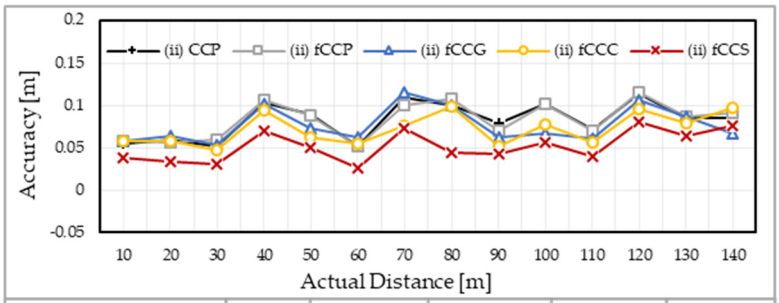
4.3. Comparing the Accuracy

Figure 11 displays the accuracy comparison of the original method CCP and the four proposed methods of fCCP, fCCG, fCCC, and fCCS. Figure 11a presents the experiments in case (i) in which two methods, CCP and fCCP, have approximately equal accuracy reaching 7.052 cm and 7.051 cm, respectively. The method that has the highest accuracy reaches 4.504 cm is fCCS. The remaining methods fCCG is 6.693 cm, and fCCC is 6.195 cm. Case (ii) is presented in Figure 11b, in which CCP and fCCP also give nearly equal results of 8.254 cm and 8.286 cm, respectively. The method fCCS has the highest accuracy reaching 5.193 cm. The fCCG and fCCC methods reach 7.777 cm and 7.123 cm, respectively.



Methods	(i) CCP	(i) fCCP	(i) fCCG	(i) fCCC	(i) fCCS
Mean Accuracy (cm)	7.052	7.051	6.693	6.195	4.504
Maximum Accuracy (cm)	10.77	10.95	10.84	9.146	7.723
Minimum Accuracy (cm)	2.184	2.253	2.189	2.839	2.018

(a)



Methods	(ii) CCP	(ii) fCCP	(ii) fCCG	(ii) fCCC	(ii) fCCS
Mean Accuracy (cm)	8.254	8.286	7.777	7.123	5.193
Maximum Accuracy (cm)	11.33	11.56	11.47	9.84	7.988
Minimum Accuracy (cm)	5.162	5.168	5.344	4.751	2.589

(b)

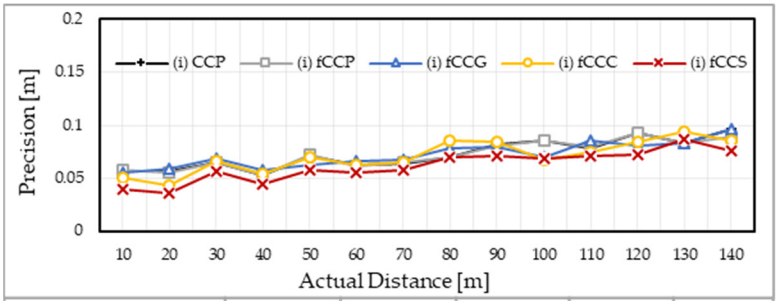
Figure 11. The accuracies of original method CCP and four proposed methods fCCP, fCCG, fCCC, and fCCS in two tested instants: (**a**) outdoor at night; (**b**) outdoor at noon.

In summary, the original method CCP and the proposed method fCCP have nearly constant accuracy in cases (i) and (ii). This proves that the proposed method has improved the processing speed significantly (as concluded in Section 4.2) but does not affect the system's accuracy. The proposed method with the highest accuracy is fCCS, with an average of 4.8 cm in two cases. However, in return, the execution time is ten times slower than the other three proposed methods of fCCP, fCCG, and fCCC.

4.4. Comparing the Precision

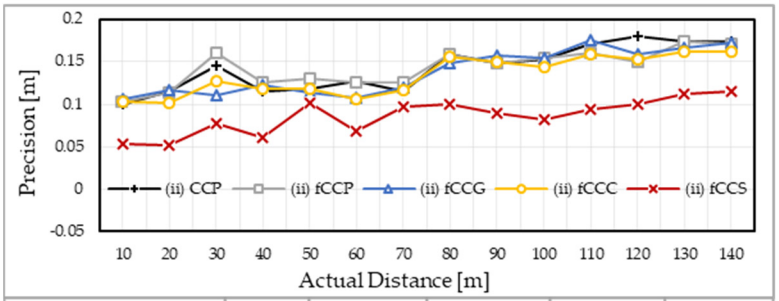
Figure 12 depicts the precision results of the proposed methods for evaluation in this study. Figure 12a compares the precision in experimental case (i). The results show that the CCP has an average precision of 7.262 cm, which is close equal to the fCCP method of 7.235 cm. In this case, the method with the highest precision is fCCS reaches 6.184 cm. The remaining fCCG and fCCC are 7.242 cm and 7.068 cm, respectively. In the tested case

(ii) shown in Figure 12b. This experiment also shows that the CCP and fCCP give nearly equal precision, with CCP of 14.259 cm and fCCP of 14.295 cm. Furthermore, the fCCG method has a value of 13.78 cm, and the fCCC is 13.410 cm. The fCCS method has the highest precision of 8.588 cm.



Methods	(i) CCP	(i) fCCP	(i) fCCG	(i) fCCC	(i) fCCS
Mean Precision (cm)	7.262	7.235	7.242	7.068	6.184
Maximum Precision (cm)	9.64	9.252	9.654	9.374	8.7
Minimum Precision (cm)	5.316	5.331	5.531	4.362	3.615

(a)



Methods	(ii) CCP	(ii) fCCP	(ii) fCCG	(ii) fCCC	(ii) fCCS
Mean Precision (cm)	14.259	14.295	13.780	13.410	8.588
Maximum Precision (cm)	18.073	17.458	17.537	16.189	11.528
Minimum Precision (cm)	10.032	10.267	10.62	10.17	5.189

(b)

Figure 12. The precisions of the original method CCP and four proposed methods fCCP, fCCG, fCCC, and fCCS in two experiment cases: (**a**) outdoors at night; (**b**) outdoors at noon.

In conclusion, CCP and the proposed method fCCP gain nearly similar precision results in each experimental case. It also shows that the proposed method does not affect the precision of the measurements. The method with the highest precision in both cases (i) and (ii) is fCCS.

4.5. Compare the Results with Performance of Commercial LiDARs and Recent Research

In this section, we evaluate the performance of the proposed methods by comparing our results with some of the latest commercial LiDAR products and a recent study.

A typical 2D LiDAR product RPLiDAR-A3 of the Slamtec company can measure distances up to 25 m with 25% accuracy and achieve a speed of 16,000 points per second [48]. In addition, Velodyne is a famous 3D LiDAR manufacturer with the newest product Ultra-puck, which can estimate distances up to 200 m and an accuracy of 2 cm [49]. The Ultra-puck uses 32 laser beams for scanning at the same time with a speed that reaches 600,000 points per second. Our LiDAR system only utilizes a single-laser beam and can achieve a rate of 879 ns per measurement. With this result, our LiDAR system achieves a speed of 1,137,656 points per second which is many times higher than today's commercial products.

In the study [47], the authors used an analog-to-digital converter (ADC) that has a sampling rate of 1.25 Giga samples per second with a resolution of 0.8 ns (1.2 cm). It is

ten times higher than our ADC of 125 Msps with 8 ns (1.2 m) resolution. This means that accuracy/precision should be ten times higher than our system. However, the results of this article only achieve an accuracy/precision of 4.9 cm/10.4 cm (with SNR =18.4 dB), which is close to our result of 8.286 cm/14.295 cm (with the fCCP method in case of SRN = −9.1 dB). Furthermore, our experiments performed under high noise conditions with SNR −9.1 dB achieved a rate of 879 ns per measurement, which is several times faster than the authors' experiments [47] with 8.7 µs per measurement under the condition of 18.4 dB.

5. Discussion

Based on the obtained results from our contributions above, this discussion addresses two important problems of our proposal: the efficiency of the proposed methods and the effect of interpolation methods on the execution time of the measurements.

Compared with the pulse edge detection methods (DToF), the cross-correlation (CC) method (IToF) is applied to the full signal form, which contains most of the information from the received signal, so it is used very effectively in high noise environments. Furthermore, the CC method implements the cross-correlation function that can fix the original emitted signal with the received signal to increase the accuracy of measurements. However, a drawback of the CC method is the computational volume is large, so the processing speed is slow. Relied on the important properties that the noise from the outside environment is random and the position of stop pulses is constant in the same distance, we perform parallel addition of stop pulses to distinguish between actual stop pulse and background noise. Furthermore, LiDAR-Pulse has a very narrow pulse shape in an emitted cycle, so it only needs to apply the correlation function to the narrow pulse segment of the start signal and the sum of the stop signals. In this way, we have proposed the fast CC algorithm that significantly improves the processing speed compared to the original CC method when combined with the same interpolation method.

The second issue of discussion is the influence of applying interpolation methods to increase the accuracy of measurements. In order to reduce the cost and amount of data to compute, the ADCs used are limited to a resolution of 8 ns (1.2 m) per sample, so it is necessary to utilize interpolation techniques to increase the accuracy of measurements. Among the interpolation methods applied and evaluated, the fCCS has the highest accuracy/precision because it is applied with many interpolated points to make the curve fixed with the original pulse. However, the amount of calculations in this method is large, so it greatly affects the execution time of the system. The remaining three methods fCCP, fCCG, and fCCC, have lower accuracy/precision than fCCS; however, when looking at the results, this difference is not significant. In contrast, the average execution time of these three methods is ten times faster than fCCS since they exclusively calculate one peak value of the interpolation curve based on the three highest points of the CCF function. The fCCP has the quickest processing time in the proposed methods because the formula for finding the peak value is the simplest. The fCCP is also the method that responds to the processing speed and accuracy requirements that we will apply to a low-cost and high-performance LiDAR system based on integrated system-on-chip technology in the future.

6. Conclusions

This study proposed a solution to improve the execution speed of measurements and evaluated the combination of the proposed algorithm with interpolation methods in enhancing the accuracy of the LiDAR system operating in high background noise environments. To test the proposed solutions, we experimented on a real-time LiDAR system and conducted trials outdoor in conditions with light noise intensities of −3 dB and −9.1 dB. Experiments were implemented at varying distances from 10 m to 140 m with each movement step of 10 m. The results obtained in the case of strong noise show that the proposed method fCCP achieves the highest speed of 879 ns, which is thirty-eight times faster than the original method CCP of 33.5 µs. Moreover, with the ADCs having a resolution of 1.2 m, the proposed method has the highest accuracy/precision is fCCS of

5.193 cm/8.588 cm. The proposed methods fCCP, fCCG, and fCCC, respectively, have the accuracy/precision of 8.286 cm/14.295 cm, 7.777 cm/13.780 cm, and 7123 cm/13.410 cm, which are lower than the fCCS method and is not significant. In contrast, these three methods have processing speeds ten times quicker than fCCS. Therefore, the fCCP, fCCG, and fCCC not only respond well to processing speed but also ensure measurement accuracy. These results demonstrate that our proposed methods significantly improve the processing speed and accuracy/precision of the measurements which respond to real-time LiDAR system designs achieving high resolution and performance.

Author Contributions: Conceptualization, T.-T.N. and C.-H.C.; methodology, T.-T.N.; software, T.-T.N. and M.-H.L.; validation, T.-T.N., C.-H.C. and D.-G.L.; results analysis, T.-T.N.; writing—original draft preparation, T.-T.N.; writing, reviewing, and editing, C.-H.C. and D.-G.L.; supervision, C.-H.C.; funding acquisition, C.-H.C. All authors have read and agreed to the published version of the manuscript.

Funding: We are glad thankful for the support of the research fund from Ministry of Science and Technology, Taiwan, under contract No. 109-2218-E-035-005.

Acknowledgments: The authors would like to thank the National Yang Ming Chiao Tung University, Taiwan for the SPAD sensor supporting this research.

Conflicts of Interest: The authors declare no conflict of interest.

References

1. Badue, C.; Guidolini, R.; Carneiro, R.V.; Azevedo, P.; Cardoso, V.B.; Forechi, A.; Jesus, L.; Berriel, R.; Paixão, T.M.; Mutz, F.; et al. Self-driving cars: A survey. *Expert Syst. Appl.* **2019**, *165*, 113816. [CrossRef]
2. Vargas, J.; Alsweiss, S.; Toker, O.; Razdan, R.; Santos, J. An overview of autonomous vehicles sensors and their vulnerability to weather conditions. *Sensors* **2021**, *21*, 5397. [CrossRef] [PubMed]
3. Zang, S.; Ding, M.; Smith, D.; Tyler, P.; Rakotoarivelo, T.; Kaafar, M.A. The Impact of Adverse Weather Conditions on Autonomous Vehicles: How Rain, Snow, Fog, and Hail Affect the Performance of a Self-Driving Car. *IEEE Veh. Technol. Mag.* **2019**, *14*, 103–111. [CrossRef]
4. Hecht, J. Lidar for Self-Driving Cars. *Opt. Photonics News* **2018**, *29*, 26–33. [CrossRef]
5. Chavez-Garcia, R.O.; Aycard, O. Multiple Sensor Fusion and Classification for Moving Object Detection and Tracking. *IEEE Trans. Intell. Transp. Syst.* **2016**, *17*, 525–534. [CrossRef]
6. Zhao, M.; Mammeri, A.; Boukerche, A. Distance measurement system for smart vehicles. In Proceedings of the 2015 7th International Conference on New Technologies, Mobility and Security (NTMS), Paris, France, 27–29 July 2015; pp. 1–5. [CrossRef]
7. Bengler, K.; Dietmayer, K.; Farber, B.; Maurer, M.; Stiller, C.; Winner, H. Three decades of driver assistance systems: Review and future perspectives. *IEEE Intell. Transp. Syst. Mag.* **2014**, *6*, 6–22. [CrossRef]
8. Khairul, I.; Bhuiyan, A. *LiDAR Sensor for Autonomous Vehicle*; Technical Report; Technische Universität Chemnitz: Chemnitz, Germany, 2017. [CrossRef]
9. Behroozpour, B.; Sandborn, P.A.M.; Wu, M.C.; Boser, B.E. Lidar System Architectures and Circuits. *IEEE Commun. Mag.* **2017**, *55*, 135–142. [CrossRef]
10. Rapp, J.; Tachella, J.; Altmann, Y.; McLaughlin, S.; Goyal, V.K. Advances in Single-Photon Lidar for Autonomous Vehicles: Working Principles, Challenges, and Recent Advances. *IEEE Signal. Process. Mag.* **2020**, *37*, 62–71. [CrossRef]
11. Sun, W.; Hu, Y.; MacDonnell, D.G.; Weimer, C.; Baize, R.R. Technique to separate lidar signal and sunlight. *Opt. Express* **2016**, *24*, 12949. [CrossRef]
12. Hao, Q.; Cao, J.; Hu, Y.; Yang, Y.; Li, K.; Li, T. Differential optical-path approach to improve signal-to-noise ratio of pulsed-laser range finding. *Opt. Express* **2014**, *22*, 563. [CrossRef]
13. Cheng, Y.; Cao, J.; Hao, Q.; Xiao, Y.; Zhang, F.; Xia, W.; Zhang, K.; Yu, H. A novel de-noising method for improving the performance of full-waveform LiDAR using differential optical path. *Remote Sens.* **2017**, *9*, 1109. [CrossRef]
14. Beer, M.; Haase, J.F.; Ruskowski, J.; Kokozinski, R. Background light rejection in SPAD-based LiDAR sensors by adaptive photon coincidence detection. *Sensors* **2018**, *18*, 4338. [CrossRef] [PubMed]
15. Li, H.; Chang, J.; Xu, F.; Liu, Z.; Yang, Z.; Zhang, L.; Zhang, S.; Mao, R.; Dou, X.; Liu, B. Efficient lidar signal denoising algorithm using variational mode decomposition combined with a whale optimization algorithm. *Remote Sens.* **2019**, *11*, 126. [CrossRef]
16. Mei, L.; Zhang, L.; Kong, Z.; Li, H. Noise modeling, evaluation and reduction for the atmospheric lidar technique employing an image sensor. *Opt. Commun.* **2018**, *426*, 463–470. [CrossRef]
17. Zhou, M.; Li, C.R.; Ma, L.; Guan, H.C. Land cover classification from full-waveform Lidar data based on support vector machines. *Int. Arch. Photogramm. Remote Sens. Spat. Inf. Sci. ISPRS Arch.* **2016**, *41*, 447–452. [CrossRef]
18. Agishev, R.; Gross, B.; Moshary, F.; Gilerson, A.; Ahmed, S. Simple approach to predict APD/PMT lidar detector performance under sky background using dimensionless parametrization. *Opt. Lasers Eng.* **2006**, *44*, 779–796. [CrossRef]

19. Fersch, T.; Weigel, R.; Koelpin, A. Challenges in miniaturized automotive long-range lidar system design. In *Three-Dimensional Imaging, Visualization, and Display 2017*; International Society for Optics and Photonics: Bellingham, WA, USA, 2017; Volume 10219, p. 102190T. [CrossRef]
20. Nguyen, T.; Cheng, C.; Liu, D.; Le, M. Improvement of Accuracy and Precision of the LiDAR System Working in High Background Light Conditions. *Electronics* **2022**, *11*, 45. [CrossRef]
21. Lai, X.; Torp, H. Interpolation methods for time-delay estimation using cross-correlation method for blood velocity measurement. *IEEE Trans. Ultrason. Ferroelectr. Freq. Control* **1999**, *46*, 277–290. [CrossRef]
22. Luciano, N.B.; Alberto, S.C.J.; Carlos, P.O.J.; Manuel, R.A.J. Development of an ultrasonic thickness measurement equipment prototype. In Proceedings of the 2010 20th International Conference on Electronics Communications and Computers (CONIELECOMP), Cholula, Mexico, 22–24 February 2010; pp. 124–129. [CrossRef]
23. Tsai, W.Y.; Huang, C.F.; Liao, T.L. New implementation of high-precision and instant-response air thermometer by ultrasonic sensors. *Sens. Actuators A Phys.* **2005**, *117*, 88–94. [CrossRef]
24. Padmanabhan, P.; Zhang, C.; Charbon, E. Modeling and analysis of a direct time-of-flight sensor architecture for LiDAR applications. *Sensors* **2019**, *19*, 5464. [CrossRef]
25. Tontini, A.; Gasparini, L.; Perenzoni, M. Numerical model of spad-based direct time-of-flight flash lidar CMOS image sensors. *Sensors* **2020**, *20*, 5203. [CrossRef] [PubMed]
26. Zhang, C.; Lindner, S.; Antolovic, I.M.; Mata Pavia, J.; Wolf, M.; Charbon, E. A 30-frames/s, 252 × 144 SPAD Flash LiDAR with 1728 Dual-Clock 48.8-ps TDCs, and Pixel-Wise Integrated Histogramming. *IEEE J. Solid-State Circuits* **2019**, *54*, 1137–1151. [CrossRef]
27. Kao, Y.H.; Chu, T.S. A Direct-Sampling Pulsed Time-of-Flight Radar With Frequency-Defined Vernier Digital-to-Time Converter in 65 nm CMOS. *IEEE J. Solid-State Circuits* **2015**, *50*, 2665–2677. [CrossRef]
28. Hoseini, M.R.; Wang, X.; Zuo, M.J. Estimating ultrasonic time of flight using envelope and quasi maximum likelihood method for damage detection and assessment. *Meas. J. Int. Meas. Confed.* **2012**, *45*, 2072–2080. [CrossRef]
29. Shaswary, E.; Tavakkoli, J.; Xu, Y. A new algorithm for time-delay estimation in ultrasonic echo signals [Correspondence]. *IEEE Trans. Ultrason. Ferroelectr. Freq. Control* **2015**, *62*, 236–241. [CrossRef]
30. Li, X.; Yang, B.; Xie, X.; Li, D.; Xu, L. Influence of waveform characteristics on LiDAR ranging accuracy and precision. *Sensors* **2018**, *18*, 1156. [CrossRef]
31. Wagner, W.; Ullrich, A.; Melzer, T.; Briese, C.; Kraus, K. From Single-Pulse to Full-Waveform Scanners: Potential and Practical Challenges. *Int. Arch. Photogramm. Remote Sens. Spat. Inf. Sci.* **2004**, *35*, 201–206.
32. Shan, J.; Toth, C.K. *Topograpic Laser Ranging and Scanning: Principles and Processing*, 2nd ed.; CRC: Boca Raton, FL, USA, 2018; ISBN 9781498772273.
33. Nguyen, T.T.; Cheng, C.H.; Liu, D.G.; Tran, S.T.; Le, M.H. An Overlapping and Leading Edge Detection Combined Technique for Distance Estimation under High-Background Lights in a Pulsed-LiDAR System. In Proceedings of the 2021 3rd International Electronics Communication Conference (IECC), New York, NY, USA, 8–10 July 2021; pp. 11–16. [CrossRef]
34. Azaria, M.; Hertz, D. Time Delay Estimation by Generalized Cross Correlation Methods. *IEEE Trans. Acoust.* **1984**, *32*, 280–285. [CrossRef]
35. Li, C.; Chen, Q.; Gu, G.; Qian, W. Laser time-of-flight measurement based on time-delay estimation and fitting correction. *Opt. Eng.* **2013**, *52*, 076105. [CrossRef]
36. Reddy, V.R.; Gupta, A.; Reddy, T.G.; Reddy, P.Y.; Reddy, K.R. Correlation techniques for the improvement of signal-to-noise ratio in measurements with stochastic processes. *Nucl. Instrum. Methods Phys. Res. Sect. A Accel. Spectrom. Detect. Assoc. Equip.* **2003**, *501*, 559–575. [CrossRef]
37. Nguyen, T.H.; Chabah, M.; Sintes, C. Correlation bias analysis—A novel method of sinus cardinal model for least squares estimation in cross-correlation. In Proceedings of the OCEANS 2015—MTS/IEEE Washington, Washington, DC, USA, 19–22 October 2015. [CrossRef]
38. Céspedes, I.; Huang, Y.; Ophir, J.; Spratt, S. Methods for Estimation of Subsample Time Delays of Digitized Echo Signals. *Ultrason. Imaging* **1995**, *17*, 142–171. [CrossRef] [PubMed]
39. Viola, F.; Walker, W.F. A spline-based algorithm for continuous time-delay estimation using sampled data. *IEEE Trans. Ultrason. Ferroelectr. Freq. Control* **2005**, *52*, 80–93. [CrossRef] [PubMed]
40. Svilainis, L.; Lukoseviciute, K.; Dumbrava, V.; Chaziachmetovas, A. Subsample interpolation bias error in time of flight estimation by direct correlation in digital domain. *Meas. J. Int. Meas. Confed.* **2013**, *46*, 3950–3958. [CrossRef]
41. Svilainis, L. Review on Time Delay Estimate Subsample Interpolation in Frequency Domain. *IEEE Trans. Ultrason. Ferroelectr. Freq. Control* **2019**, *66*, 1691–1698. [CrossRef] [PubMed]
42. Leica DISTO Lite 5 Laser Distance Meter. Available online: https://www.libble.eu/leica-disto-lite-5/online-manual-794280/ (accessed on 25 January 2022).
43. Viola, F.; Walker, W.F. Computationally efficient spline-based time delay estimation. *IEEE Trans. Ultrason. Ferroelectr. Freq. Control* **2008**, *55*, 2084–2091. [CrossRef]
44. Pinton, G.F.; Trahey, G.E. Continuous delay estimation with polynomial splines. *Proc. IEEE Ultrason. Symp.* **2006**, *1*, 1702–1705. [CrossRef]

45. Ryan, M. *Computational Nuclear Engineering and Radiological Science Using Python*; Elsevier: Amsterdam, The Netherlands, 2018; ISBN 9780128122532.
46. Kong, Q.; Siauw, T.; Bayen, A.M. *Python Programming and Numerical Methods*; Academic Press: Cambridge, MA, USA, 2021; ISBN 9780128195499.
47. Xie, X.; Xu, L.; Wang, Z.; Li, X. Real-Time in Situ Laser Ranging Based on Online Echo Waveform Fitting. *IEEE Sens. J.* **2019**, *19*, 9255–9262. [CrossRef]
48. RPLiDAR A3. Available online: https://www.slamtec.com/en/Lidar/A3 (accessed on 2 March 2022).
49. Ultra-Puck LiDAR. Available online: https://velodynelidar.com/products/ultra-puck/ (accessed on 2 March 2022).